AIAA JOURNAL
Vol. 38, No. 11, November 2000

Effects of Spatial Filtering on Sound Radiation from a Subsonic Axisymmetric Jet

Wei Zhao,* Steven H. Frankel,† and Luc Mongeau‡
Purdue University, West Lafayette, Indiana 47907

The effects of spatial filtering on the sound generated from a subsonic axisymmetric jet were investigated by filtering near-field flow variables obtained from a direct numerical simulation. This is useful to assess the accuracy of the large-eddy simulation (LES) technique for predicting aerodynamically generated sound. Lighthill's acoustic analogy in the frequency domain was employed to predict the far-field sound. The direct numerical simulation results were in excellent agreement with recently published results for the same jet (Mitchell, B. E., Lele, S. K., and Moin, P., "Direct Computation of the Sound Generated by Vortex Pairing in an Axisymmetric Jet," *Journal of Fluid Mechanics*, Vol. 383, 1999, pp. 113–142). To handle the effects of domain truncation errors on the Lighthill source term, a windowing function was employed. Predictions of the far-field sound using Lighthill's acoustic analogy were in good agreement with the simulation results at low frequencies, even for shallow angles from the jet axis. Significant discrepancies were observed at high frequencies. It was found that low-frequency sound was dominant and the effects of filtering on the low-frequency sound were negligible. In addition, the sound levels computed from both the filtered and unfiltered source terms were in good agreement with the directly computed results. Filtering reduced the small-scale fluctuations in the near-field and, as expected, decreased the magnitude of the source term for the high-frequency sound. A model was developed and tested to predict the subgrid contribution to the Lighthill tensor in cases where, as in LES, only relatively large-scale flow structures are resolved.

I. Introduction

FLOW-GENERATED sound is important in many engineering and physiological applications. Traditionally, the field of aeroacoustics has been explored experimentally by measuring the far-field sound radiated by a particular flow configuration, or analytically by seeking theories to relate detailed near-field flow phenomena to the far-field sound. Recent advances in computer performance and computational methods have generated great interest in the study of aeroacoustics using computational aeroacoustics (CAA) methods.

One powerful CAA method is direct numerical simulation (DNS), in which all turbulent scales of motion are resolved. However, the computational cost, which is proportional to the third power of Reynolds number,[1] limits its application to low Reynolds number flows and simple geometries. A compromise alternative to DNS is large-eddy simulation (LES). In LES, the large scales are numerically simulated, while the small, subgrid scales (SGS) are modeled. Because the latter depend essentially on fluid viscosity and tend to be more homogeneous than the large coherent eddies, their effect on the resolved large scales can presumably be modeled fairly accurately.

There have been several recent studies in the literature that have employed DNS or LES to study aerodynamically generated sound, which are of relevance to the present study. In Ref. 2, the unsteady compressible Navier–Stokes equations were solved in two dimensions for a planar jet in the context of a semideterministic turbulence model and Lighthill's acoustic analogy for the far-field sound. They effectively used a standard κ–ϵ turbulence model with a reduced empirical constant premultiplying the eddy viscosity to model the fine-grained turbulence. Their findings suggest that, for subsonic jets, the far-field sound is due to emissions from the large-scale coherent structures, whereas high-frequency radiation is due to smaller eddies contained within these large-scale structures. They suggest the use of fully three-dimensional LES to address this issue. In Ref. 3, a compressible LES model for the near-field was coupled to the Kirchhoff method to predict supersonic jet noise. Gamet and Estivalezes did not directly discuss the problem of the contribution of small scales on radiated sound. They suggested, however, that LES must be performed in a three-dimensional coordinate system, as opposed to a two-dimensional axisymmetric one, to address this issue. Most recently, in Ref. 4 [Mitchell, Lele, and Moin (MLM)], DNS results for both subsonic and supersonic axisymmetric jets were analyzed to study the role of vortex pairing in jet sound generation. Kirchhoff's method and Lighthill's approach to predict the far-field sound were also used. The findings of Mitchell et al.[4] were in qualitative agreement with previous experimental data. Mitchell et al. also addressed the issue of domain truncation on the Lighthill tensor and its impact on the application of Lighthill's acoustic analogy to such flows. In Ref. 5, an a priori analysis of DNS results for a turbulent channel flow was conducted to examine the effects of small scales on the source term in Lighthill's acoustic analogy. Piomelli et al.[5] found that filtering the Lighthill tensor and, thus, removing small scales did not affect the spatial distribution of the tensor but did affect the higher derivatives. They also suggested that a model could be developed for small-scale sound based on homogeneous isotropic turbulence theory. They did not actually compute the far-field sound using the filtered Lighthill tensor and a solution to Lighthill's equation. In Ref. 6, an a priori analysis of the contribution of the SGS motions to sound production in decaying isotropic turbulence was presented. Seror et al. demonstrated that the unresolved fluctuations do not contribute significantly to the emitted sound intensity. They showed this effect by employing both a Smagorinsky model and a scale-similarity model for the SGS stress tensor in their sound predictions. They showed that the scale-similarity model for the SGS tensor was preferred over the Smagorinksy model. They did not attempt to model the contribution of the smallest scales to the radiated sound. Previous studies clearly suggest that an LES model coupled to a model for the far-field sound, such as Lighthill's analogy, is a sensible approach to aeroacoustic jet noise predictions; however, important issues should be addressed, including 1) the effect of the spatial filtering on the generation of far-field sound and 2) the large spatial extent of the Lighthill tensor. These issues will be examined for a subsonic axisymmetric jet in this paper.

In this paper, results are presented from a direct computation of sound generated by a harmonically forced axisymmetric jet of Mach number 0.4. The results are in good agreement with the numerical results of MLM.[4] Later in this paper, the effects of spatial filtering on the sound radiation are studied using a priori analysis. The DNS

Received 4 June 1999; revision received 29 March 2000; accepted for publication 10 April 2000.

*Ph.D. Student, School of Mechanical Engineering.
†Associate Professor, School of Mechanical Engineering. Senior Member AIAA.
‡Associate Professor, School of Mechanical Engineering. Member AIAA.

near-field data are filtered with a top-hat filter, and Lighthill's acoustic analogy is applied to predict far-field sound. A new approach for handling the large spatial extent of the Lighthill tensor is also tested and a model for the SGS sound contribution is developed. Note that ideally a fully three-dimensional DNS of the near and far field of a freejet would be preferred to address these issues, but this is computationally prohibitive. Although the extent of spatial scales in the current DNS of an axisymmetric jet is not as large as in a real turbulent jet, we do observe a difference of at least one order between the small and large scales. The filter width used is close to the smallest scales in the current jet. The filter reduces the small-scale fluctuations significantly, although it does not remove them completely.

The paper is organized as follows: In Sec. II, the mathematical formulation, including the DNS and filtered LES equations, and the Lighthill's acoustic analogy formulation are presented. The details of the numerical methods used are also described in Sec. II. Results are presented and discussed in Sec. III. Conclusions are drawn in Sec. IV.

II. Governing Equations

A. DNS Equations

The compressible Navier–Stokes equations in a Cartesian coordinate system have the form

$$\frac{\partial \rho}{\partial t} + \frac{\partial \rho u_j}{\partial x_j} = 0 \tag{1}$$

$$\frac{\partial \rho u_i}{\partial t} + \frac{\partial \rho u_i u_j}{\partial x_j} = -\frac{\partial p}{\partial x_i} + \frac{\partial \sigma_{ij}}{\partial x_j} \tag{2}$$

$$\frac{\partial e}{\partial t} + \frac{\partial (e + p) u_j}{\partial x_j} = -\frac{\partial q_j}{\partial x_j} + \frac{\partial u_k \sigma_{kj}}{\partial x_j} \tag{3}$$

where

$$e = \tfrac{1}{2}\rho u_k u_k + [1/(\gamma - 1)]p \tag{4}$$

$$\sigma_{ij} = \mu\left(\frac{\partial u_i}{\partial x_j} + \frac{\partial u_j}{\partial x_i}\right) - \frac{2}{3}\mu\frac{\partial u_k}{\partial x_k}\delta_{ij} \tag{5}$$

$$q_j = -k\frac{\partial T}{\partial x_j} \tag{6}$$

where j takes on values of 1, 2, and 3 for the three Cartesian coordinate directions x, y, and z; p is pressure; u_j is velocity component; and e is the total specific energy. An ideal, calorically perfect gas with constant specific heats was assumed. The specific heat ratio $\gamma = c_p/c_v$ was 1.4. The dynamic viscosity μ and coefficient of thermal conductivity k were assumed to be constant with a Prandtl number $Pr = \mu c_p/k = 1.0$.

For the axisymmetric jet problem in this study, it was assumed that $v_\phi = 0$ (nonswirling flow) and $\partial f/\partial\phi = 0$, where ϕ is the azimuthal coordinate, v_ϕ is the velocity component in azimuthal direction, and f is an arbitrary function. When the Navier–Stokes equations in a Cartesian coordinate system are applied to axisymmetric problems, the preceding relations can be used to recast the derivatives along the z direction in terms of variables and derivatives in the x–y plane, where y and z are in the same coordinates as r and ϕ, respectively. With the Cartesian coordinate system being used everywhere, the centerline $y = 0$ is no longer a singular axis, whereas it is in the cylindrical coordinate system.

B. Filtered Navier–Stokes Equations

In LES, any flow variable, for example, f, can be decomposed into a resolved or filtered part $\bar{f}$ and an unresolved or subgrid part f', yielding $f = \bar{f} + f'$. The filtering operation, indicated by the overbar, in LES is achieved with a convolution integral given by

$$\bar{f}(\boldsymbol{x}) = \int_D G(\boldsymbol{x} - \boldsymbol{y}) f(\boldsymbol{y})\, \mathrm{d}\boldsymbol{y} \tag{7}$$

where G is the filter function and D represents the entire computational domain. In this study, we used a top-hat filter in physical space defined by

$$G(x) = \begin{cases} 1/\bar{\Delta} & \text{if} \quad |x| \le \bar{\Delta}/2 \\ 0 & \text{otherwise} \end{cases} \tag{8}$$

where $\bar{\Delta}$ is the filter width. In compressible flows, it is convenient to use Favre filtering to avoid subgrid-scale terms in the continuity equation. A Favre-filtered variable is defined as

$$\tilde{f} = \overline{\rho f}/\bar{\rho} \tag{9}$$

Applying this filtering operation to the Navier–Stokes equations, we obtain the Favre-filtered Navier–Stokes equations, which take the form

$$\frac{\partial \bar{\rho}}{\partial t} + \frac{\partial}{\partial x_j}(\bar{\rho}\widetilde{u_j}) = 0 \tag{10}$$

$$\frac{\partial}{\partial t}(\bar{\rho}\tilde{u}_i) + \frac{\partial}{\partial x_j}(\bar{\rho}\widetilde{u_i}\widetilde{u_j}) = -\frac{\partial \bar{p}}{\partial x_i} - \frac{\partial \tau_{ij}}{\partial x_j} + \frac{\partial \tilde{\sigma}_{ij}}{\partial x_j} \tag{11}$$

where $\tilde{\sigma}_{ij}$ is the resolved viscous stress tensor and where

$$\tau_{ij} = \bar{\rho}\widetilde{u_i u_j} - \bar{\rho}\widetilde{u_i}\widetilde{u_j} \tag{12}$$

is the SGS stress tensor, which must be modeled in an actual LES. Note that the filtered energy equation is not presented here because it is not used in the derivation of Lighthill's acoustic analogy.

C. Lighthill's Acoustic Analogy

Lighthill's acoustic analogy involves a rearrangement of the compressible Navier–Stokes equations to derive a nonhomogeneous wave equation for an acoustic variable. The nonhomogeneous term on the right-hand side of the derived wave equation is interpreted as a distribution of acoustic sources in a quiescent ambient. The theory and derivation of Lighthill's equation is given by Lighthill.[7] Combining the time derivative of the continuity equation (2) with the divergence of the momentum equation (3) yields

$$\frac{\partial^2 \rho'}{\partial t^2} - c_\infty^2 \nabla^2 \rho' = \frac{\partial^2 T_{ij}}{\partial x_i \partial x_j} \tag{13}$$

with the Lighthill tensor T_{ij} defined as

$$T_{ij} = \rho u_i u_j + \delta_{ij}\left(p' - c_\infty^2 \rho'\right) - \sigma_{ij} \tag{14}$$

Here $\rho' = \rho - \rho_\infty$ and $p' = p - p_\infty$, where ρ_∞, p_∞, and c_∞ are the density, pressure, and sound speed in the far field, respectively. Equation (13) is exact, in the sense that no approximations to the Navier–Stokes equations have been made. However, the analogy is not complete unless two conditions are met: First, $T_{ij} = 0$ in the region where the sound is to be predicted, that is, the acoustic medium is a region where c_∞ is constant and there is no mean flow, and, second, there exists a way to compute T_{ij} independently of Eq. (13).

When DNS is used to simulate the flowfield, the calculation of Lighthill's tensor T_{ij} is straightforward, and Eq. (13) can then be integrated to predict the far-field sound. But when LES is employed to predict the near field, only the resolved or large-scale contribution to T_{ij} is available. To clarify this, the unfiltered Lighthill tensor T_{ij} can be decomposed into a resolved, $\bar{T}_{ij}$, and a subgrid, T'_{ij}, part as follows:

$$T_{ij} = \bar{T}_{ij} + T'_{ij} \tag{15}$$

The filtered Lighthill stress tensor is obtained by combining the filtered continuity and momentum equations yielding

$$\bar{T}_{ij} = \bar{\rho}\tilde{u}_i\tilde{u}_j + \delta_{ij}\left(\bar{p}' - c_\infty^2 \bar{\rho}'\right) - \tilde{\sigma}_{ij} + \tau_{ij} \tag{16}$$

where, again, in LES a model for τ_{ij} is needed. There are two important issues involved in coupling LES for the near-field with Lighthill's analogy for the far field. These involve the relative importance of τ_{ij} and T'_{ij} to the far-field sound and potential modeling. To investigate these issues, an a priori analysis was conducted to examine the impact of spatial filtering on sound generation from a subsonic jet. The DNS results were filtered to yield the resolved and SGS fields. The exact SGS stress and the Lighthill tensor $\bar{T}_{ij}$ were then computed. This allowed the study of the physical phenomena

related to the SGS without any modeling assumptions being required. Then a model for T'_{ij} was tested. As mentioned, one would prefer to conduct a fully three-dimensional DNS of the spatially developing jet, including the far-field, to address the role of vortex stretching in generating small-scale turbulence and sound, but this is computationally prohibitive. Although LES of a spatially developing three-dimensional jet is possible,[8] information on the small scales is not available in such a simulation. Further motivation for the study of axisymmetric jets is provided by MLM.[4]

III. Numerical Methods

A. DNS Equations

The computational domain of the DNS is shown in Fig. 1. The domain begins at some distance downstream of the nozzle. The computational domain includes both the acoustic near and far fields.

A sixth-order compact central finite difference scheme was used for spatial discretization of the DNS equations.[9] A third-order compact scheme was used for the boundary points and a fourth-order scheme for points adjacent to the boundary; however, the same sixth-order compact scheme is still used at the centerline by applying symmetry or antisymmetry of a function about the centerline when computing the radial derivatives. The second-order derivatives in the viscous terms were evaluated by using two applications of the compact schemes. The standard fourth-order Runge–Kutta method was used for time integration. An explicit sixth-order compact filter was employed to eliminate sawtoothlike oscillations within the computational domain.[9]

The initial conditions for the axisymmetric jet were obtained by numerically integrating the parabolic boundary layer equations for a laminar jet. The velocity profile, given by

$$u = \frac{1}{2}U_0\left\{1 - \tanh\left[\frac{R_0}{4\delta_2}\left(\frac{r}{R_0} - \frac{R_0}{r}\right)\right]\right\} \tag{17}$$

was specified at the inlet as the starting profile for integration of the boundary layer equations. Here U_0 was the maximum velocity and $\delta_2 = 0.1R_0$ was chosen as the initial momentum thickness.

Nonreflecting boundary conditions were used in the far field.[10] An exit zone approach was used at the outflow boundary.[11] Instead of filtering the solutions in the exit zone with an explicit filter, the viscosity was artificially increased to dampen the reflections from the outflow boundary. Eigenfunctions obtained from linear stability theory[12] were used to force the jet at the inflow boundary. The frequencies chosen were the most unstable mode f_0 and its two leading subharmonics, $\frac{1}{2}f_0$ and $\frac{1}{4}f_0$.

B. Lighthill's Equation

The numerical method used to solve Lighthill's equation was similar to that used by MLM.[4] Generally, low-frequency sound is related to large-scale flow motion, and high-frequency sound is related to small-scale flow motion. Therefore, the acoustic analysis was performed in the frequency domain. The analysis begins with the temporal Fourier transform of Lighthill's equation:

$$\nabla_x^2\hat{\rho} + \left(\frac{\omega}{c_\infty}\right)^2\hat{\rho} = -\frac{1}{c_\infty^2}\frac{\partial^2}{\partial y_i \partial y_j}\hat{T}_{ij}(\mathbf{y}) \tag{18}$$

where ω is the angular frequency and $\hat{T}_{ij}$ and $\hat{\rho}$ are the Fourier components of T_{ij} and ρ', respectively. Equation (18) has a solution in terms of its Green's function, which, after some manipulations, can be written as (see Ref. 4 for details)

$$\hat{\rho}(\boldsymbol{x}) = -\frac{\omega^4}{c_\infty^2}\int_{-\infty}^{\infty}\int_0^{\infty}\int_0^{2\pi} r R_i R_j \hat{T}_{ij}\frac{e^{ikR}}{4\pi R^3}\,\mathrm{d}\phi\,\mathrm{d}r\,\mathrm{d}y_1 \tag{19}$$

in a cylindrical system, where r, ϕ, and y_1 are components of $\boldsymbol{y}$. The Eq. (19) was integrated using a second-order-accurate numerical method.

The integral volume in Eq. (19) is infinite, but in practice the computational domain has to be truncated to finite dimensions. For the jet simulations performed here, the Lighthill equation source terms are still large at the outflow boundary compared with their largest value inside the computational domain, as will be shown later. The far-field sound predictions obtained from integrating Lighthill's equation contain spurious sound waves generated by the sudden termination of source terms at the exit of the domain. MLM[4] avoided this problem by observing that the magnitudes of the source terms could be approximated by exponential decaying functions. MLM suggested using an extensive source region (passive region) attached to the DNS computational domain (active region), where the wave numbers and decaying coefficients in the passive region of the source terms are computed from the active region. The distribution of source terms in the passive region may not be easy to ascertain in general, and as a result the use of this method is limited. Nevertheless, as observed by MLM, most of the jet sound is radiated from the vortex pairing region. The flow in the region near and outside the outflow boundary does not contribute significantly to the far-field sound. A separate simulation under the same flow conditions but with a shorter computational domain (four-sevenths of the original one) has been performed. The differences between the sound radiation patterns and directivities of the simulations was very small (less than 2%). Thus, the source terms can be multiplied by a window function to smoothly damp the source terms near the boundary to zero, without sacrificing much accuracy on the sound radiation predictions. The idea is similar to the window function used in conjunction with a discrete Fourier transform to avoid the errors associated with signal nonperiodicity. The window function we adopted in this study takes the form

$$w(x) = \begin{cases} 1 & \text{if} \quad x \le x_w \\ \frac{1}{2}\{1 + \cos[(x - x_w)/(x_p - x_w)]\pi\} & \text{if} \quad x > x_w \end{cases} \tag{20}$$

where x_p is the axial position of the outflow boundary and x_w is where the window begins. Similar to the window function used in DFT, it removes only the high-wave-number components of the source terms, while allowing low-wave-number components to radiate sound. Note that we do not need a window function for the inflow boundary because the source terms at the inflow are several orders lower than the peak values.

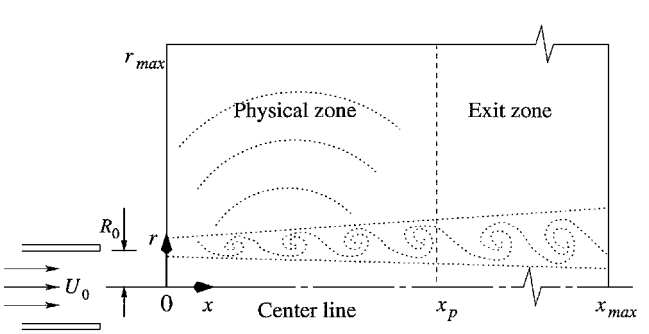

Fig. 1 Computational domain for the DNS.

IV. Results and Discussion

The jet Mach number in this computation was $M_0 = 0.4$. The Reynolds number based on the nozzle radius was 2500. The momentum thickness of the initial velocity profile was $0.1R_0$. The nondimensional fundamental frequency of the inflow forcing was $f_0R_0/U_0 = 0.218$ (Ref. 4). The dimensions of the computational domain were $x_p = 70R_0$, $r_{\max} = 80R_0$, and $x_{\max} = 250R_0$.

A 2000×304 grid was used, where the grid in the axial direction in the physical zone was uniform and the grid in the radial direction was stretched to include a sufficient number of points within the shear layer. The highest frequency resolved is estimated as $4f_0$ based on the use of seven to eight grid points per wavelength to resolve acoustic waves. The time step was specified such that the Courant–Friedrichs–Lewy number was less than 0.9. The code was parallelized using message passing interface (MPI), and the computation consumed about 1000 CPU hours on 16 processors of the SGI/Cray Origin-2000. For convenience of presenting the results, all of the flow variables were nondimensionalized by using U_0 as velocity scale and R_0 as length scale. In the next subsection, we examine the near-field and far-field DNS predictions and make comparisons to the results of MLM[4] for validation purposes.

A. DNS Results

Because of the excitation at the inflow, the jet rolls up into coherent vortical structures, which then begin to pair. Figure 2 shows a time sequence of vorticity contours for one forcing period. (The radial coordinate has been magnified by a factor of two, and only part of the computational domain, in the axial direction, is shown.) Vortex roll up and pairing can be clearly seen in Fig. 2 and are in qualitative agreement with Fig. 2 of MLM.[4] The growth of the momentum thickness δ_2 is shown in Fig. 3. A steplike increase is observed in the region of vortex pairing consistent with Fig. 3 of MLM. In this case, the jet grows at a slightly faster rate than in MLM, which is most likely due to slight differences in the initial conditions and the forcing. Other results for the time-averaged velocity profiles were also in good agreement with MLM (not shown).

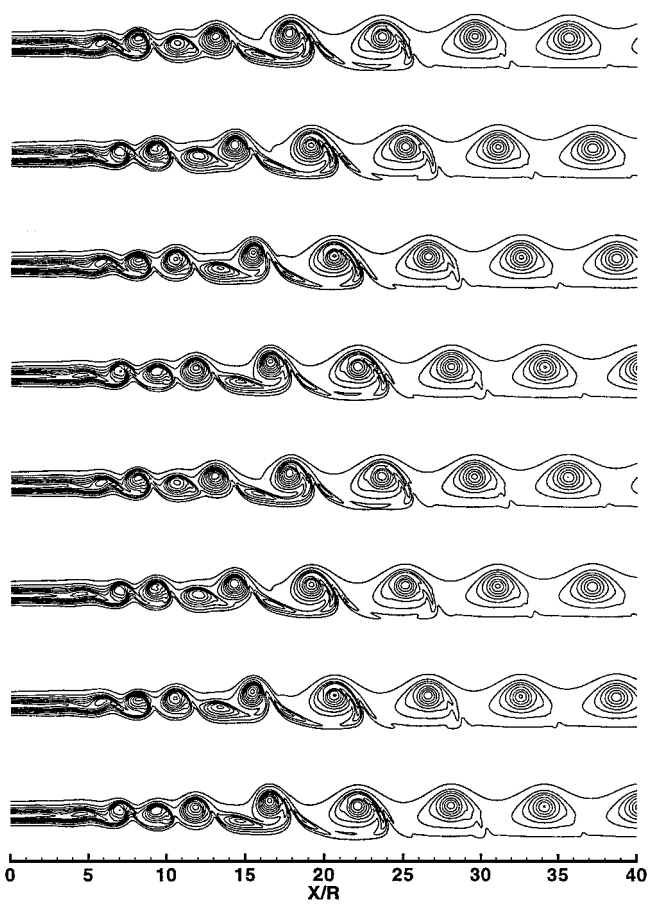

Fig. 2 Temporal sequence of vorticity contours for one forcing period, with contour levels ranging from 0 to $2.8U_0/R_0$ with increments of $0.28U_0/R_0$; $\Delta t = 1/(2f_0)$.

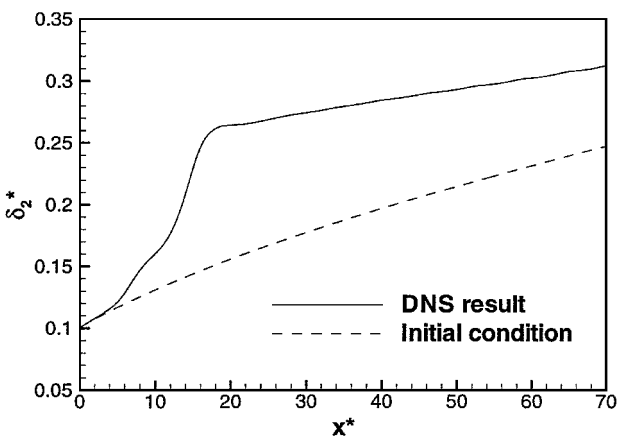

Fig. 3 Axial growth of the jet momentum thickness δ_2/R_0.

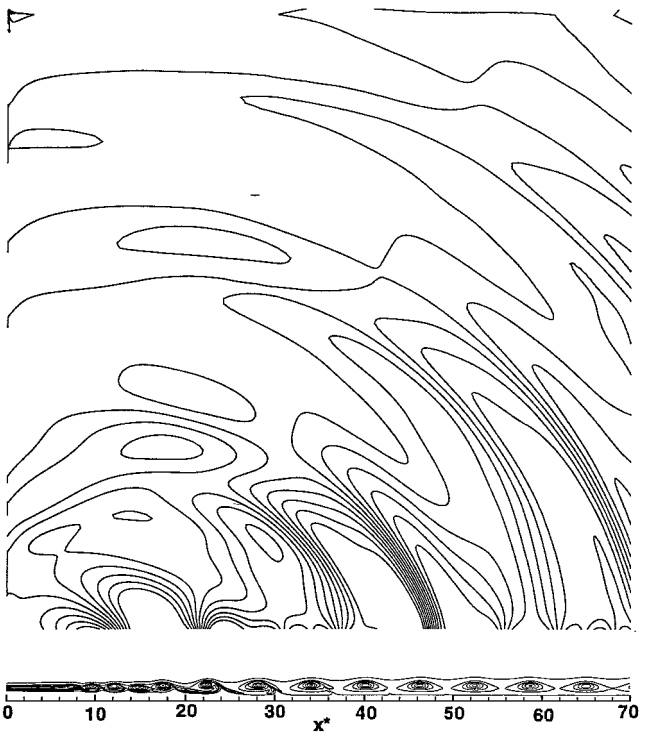

Fig. 4 Instantaneous contour plots of the far-field dilatation and near-field vorticity; contour levels for the far-field dilatation are min/max $= \mp 3 \times 10^{-6}$ with increment of 6×10^{-7}.

Traditional acoustic theory typically uses the pressure, density, or velocity potential fluctuations to describe the sound field. Unfortunately, the far-field pressure in this study did not reach a stationary mean, which is possibly related to the boundary condition treatment. However, the dilatation, $\Theta = \nabla \cdot \boldsymbol{v}$, has a fairly well-defined mean value.[4,13] Therefore, we considered the far-field dilatation when discussing the far-field sound. Note that the sound pressure can be easily obtained if the dilatation is known via

$$\frac{\partial p}{\partial t} = -\rho_\infty c_\infty^2 \Theta \tag{21}$$

Instantaneous contour plots of the near-field vorticity and far-field dilatation are shown in Fig. 4. It is observed that the dominant sound is generated in the region of vortex pairing, consistent with Fig. 7a in MLM.[4] Plots of the dilatation magnitude vs θ for different observer distances and frequencies are also in good agreement with the results of MLM (not shown). The good agreement between these DNS results and those of MLM justifies their use for a priori analysis to investigate the extensive source treatment, the effect of spatial filtering on sound prediction, and the contribution of SGS.

B. Extensive Source Treatment

To investigate the accuracy of the treatment for the extensive source term in Lighthill's analogy, values of $x_w = 45R_0$ and $x_p = 70R_0$ were used in the window function. Predictions obtained using the present approach and MLM's[4] approach for the far-field sound are compared to the directly computed results at two different frequencies in Fig. 5, where the reference source point is located at $x_s = 15.5R_0$ and $r = 0$. Both approaches are in good agreement with the DNS, but the present approach is slightly better, especially for sound waves propagating at shallow angles. The advantage of the present approach is that it can be applied in situations where the source terms in the passive region cannot be determined from the source terms in the active region. It is also very simple and inexpensive to implement.

C. Effects of Filtering

To examine the effects of filtering on the Lighthill tensor and the far-field sound, the DNS flowfields were filtered in both the axial x and radial r directions using top-hat filters with widths of three and

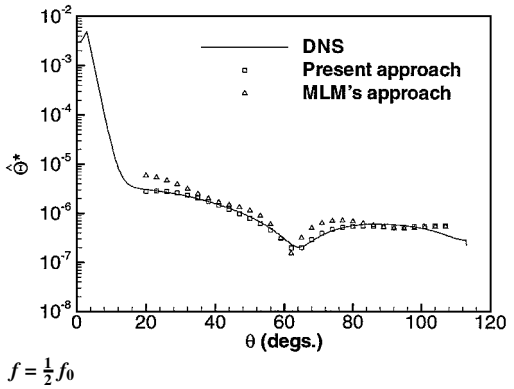

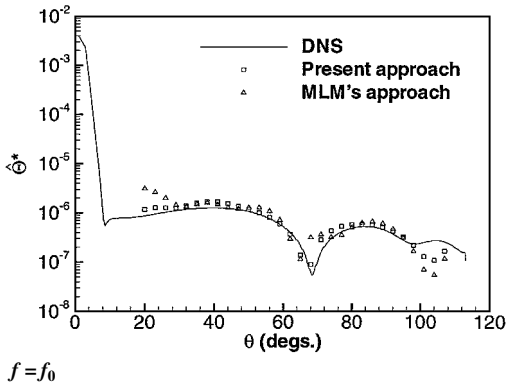

Fig. 5 Comparisons between the directly computed sound from the DNS to predictions from Lighthill's equation (symbols) using the present approach and MLM approach for an observer distance $d = 40R_0$ at two frequencies f.

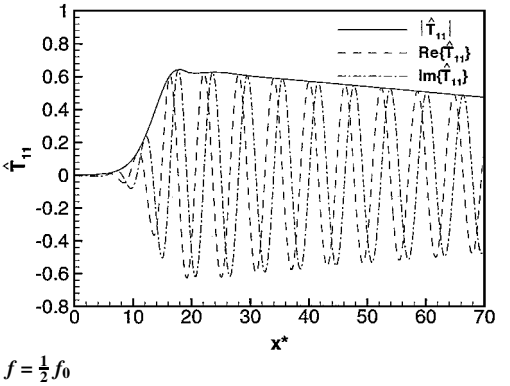

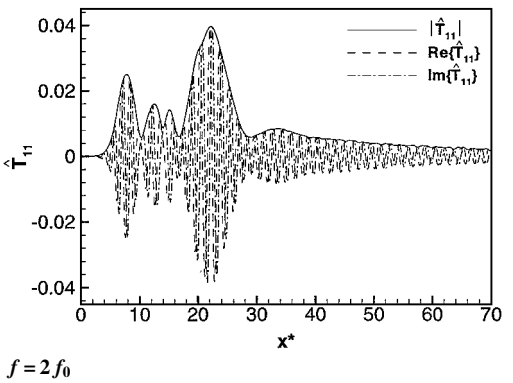

Fig. 6 Axial distribution of the real part, imaginary part, and magnitude of $\hat{T}_{11}$ at $r = 0.5R_0$ for selected frequencies.

five times the local grid spacing. The axial variation of selected terms of the unfiltered tensor $\hat{T}_{ij}$ and its magnitude $|\hat{T}_{ij}|$ at frequencies $\frac{1}{2} f_0$ and $2 f_0$ is shown in Fig. 6. In this case, $\frac{1}{2} f_0$ is the dominant frequency component, and one can see that the magnitude of the $\frac{1}{2} f_0$ component is one order higher than that of the $2 f_0$ component. For both frequencies, $\hat{T}_{ij}$ decays slowly at the outflow region. This can also be observed in contour plots of $\hat{T}_{ij}$ at the same two frequencies, as shown in Fig. 7. (Note that only part of the domain is shown and the radial coordinate has been magnified by a factor of two.) One can also observe that there exists an almost constant wavelength for each Fourier component of T_{ij} shown here. The axial wavelength of the low-frequency component is much larger than that of the high-frequency component, as expected. The wavelength of the lowest-frequency ($\frac{1}{4} f_0$) component is about 21 times that of the highest-frequency ($4 f_0$) component in this axisymmetric jet. The filtering operation should have a greater impact on the high-frequency T_{ij} components due to their short wavelength.

The directivity of the far-field sound predicted by Lighthill's acoustic analogy using $\hat{T}_{ij}$ and $\bar{\hat{T}}_{ij}$ with the exact SGS stress is shown in Fig. 8. For the lowest frequency, $\frac{1}{2} f_0$, the agreement between DNS and acoustic analogy predictions is excellent. At higher frequencies, there are discrepancies between the two predictions. The highest frequency at which the agreement is still acceptable is $2 f_0$ (only for a small range of θ). The acoustic analogy fails for frequencies higher than $2 f_0$. The poor agreement at high frequencies is expected because the solution to Lighthill's equation given by Eq. (19) does not consider the effects of refraction and dissipation as the acoustic waves propagate inside the jet shear layer. It requires the acoustic wavelength λ to be much larger than the thickness of the shear layer, which is proportional to the jet radius R_0. In this case, the acoustic wavelength at frequency $2 f_0$ is about $5.74R_0$. The requirement $R_0 \ll \lambda$ marginally holds. For higher frequencies, Lighthill's equation is no longer appropriate and a more sophisticated approach, such as Lilley's equation, may be needed.[14]

From Fig. 8, the differences between the acoustic analogy predictions using $\hat{T}_{ij}$ and $\bar{\hat{T}}_{ij}$ for frequencies $\frac{1}{2} f_0$, f_0, and $\frac{3}{2} f_0$ are small.

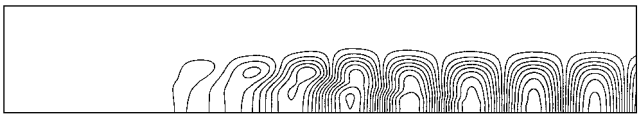

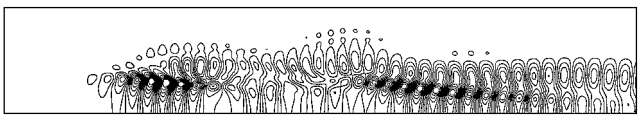

Fig. 7 Instantaneous contour plots of $\hat{T}_{11}$ at two different frequencies with 16 contour levels: a) min/max = ∓ 0.6 and b) min/max = ∓ 0.04.

The resolved stress contributes mainly to the low-frequency sound. However, for frequency $2 f_0$, a disparity between the predictions using $\hat{T}_{ij}$ and $\bar{\hat{T}}_{ij}$ begins to emerge. The smaller scales begin to make a contribution to sound whose frequency is higher than $2 f_0$.

Even though a quantitative assessment of the contribution of small scales to high-frequency sound cannot be made using Lighthill's acoustic analogy, an examination of the filtered and unfiltered Lighthill tensor field may still yield useful information on the effects of filtering on sound generation. The magnitudes of filtered and unfiltered $\hat{T}_{ij}$ terms along the axial direction are shown in Fig. 9. Again, filtering has very little effect on low-frequency stress components of $\hat{T}_{ij}$, while the magnitudes of high-frequency components are apparently reduced by filtering. For frequency $3 f_0$, the magnitude of the stress tensor decreases by about 2% when the filter width $\bar{\Delta}$ is three times the grid spacing Δ_x and 6% when $\bar{\Delta}$ is five times the grid spacing Δ_x. For frequency $4 f_0$, the magnitude decreases even more. A possible reason why the magnitudes of the high-frequency components of the Lighthill tensor do not decrease very much as a result of filtering is because the DNS is a two-dimensional computation. The axisymmetric assumption prevents the generation of fine-grained turbulence, and consequently there is very little energy in the small scales. In other words, the DNS is overresolved.

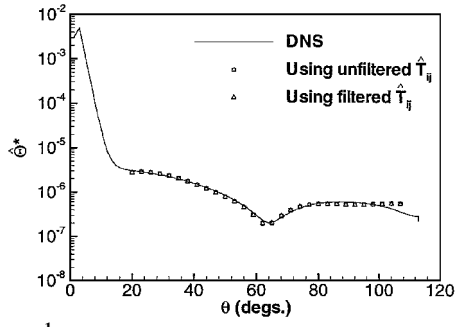

$f = \frac{1}{2} f_0$

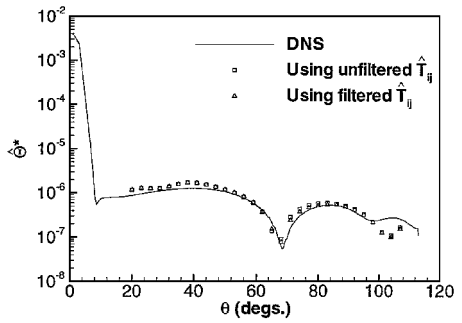

$f = f_0$

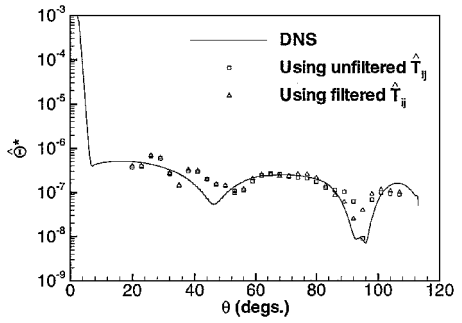

$f = \frac{3}{2} f_0$

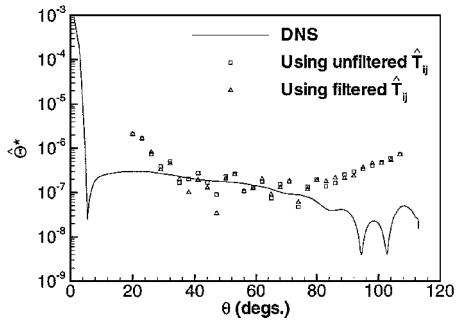

$f = 2 f_0$

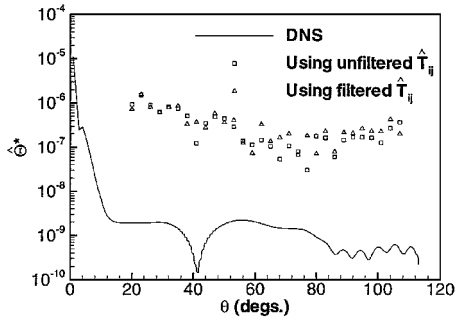

$f = 4 f_0$

Fig. 8 Predictions from Lighthill's equation for the far-field sound directivity using $\hat{T}_{ij}$ and $\tilde{T}_{ij}$ computed with exact SGS stress at selected frequencies.

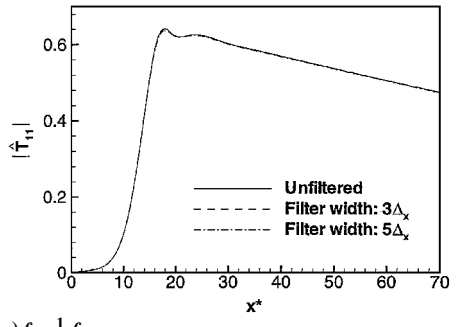

a) $f = \frac{1}{2} f_0$

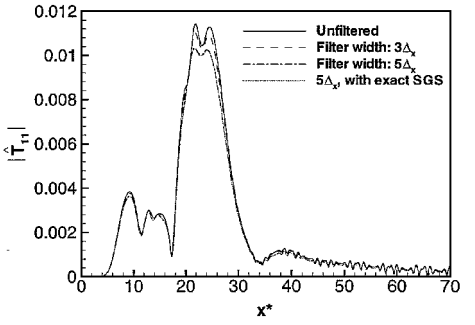

b) $f = 3 f_0$

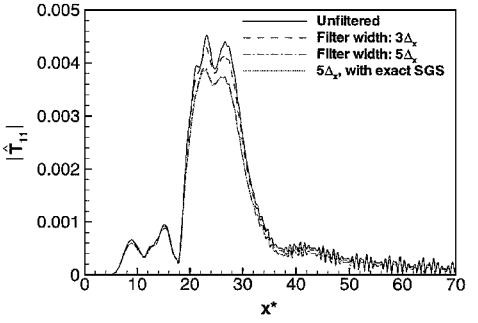

c) $f = 4 f_0$

Fig. 9 Axial variation of magnitude of $\hat{T}_{11}$, $\hat{\tilde{T}}_{11}$ without SGS stress, and $\tilde{T}_{11}$ with exact SGS stress at selected frequencies.

Note that the magnitudes of the stress tensor computed without the SGS stress and with the exact SGS stress are very close to each other (Figs. 9b and 9c). The SGS stress does not contribute significantly to sound generation in this case. With the exact SGS stress, the filtered stress tensor $\hat{\tilde{T}}_{ij}$ still is not a good approximation to the unfiltered tensor $\hat{T}_{ij}$ and is even worse than the tensor computed without SGS stress (Fig. 9c). As discussed earlier, the tensor obtained by direct filtering of the actual tensor T_{ij} is the best computed approximation to the Lighthill's tensor from the filtered flowfield; that is, the SGS model can recover the exact SGS stress. This implies that some information on the contribution of the small scales to the far-field sound is lost in LES. Recall that the SGS stress only represents the effect of small-scale motions on the large-scale motions and the details of the small scales after filtering the flowfield are unknown. Therefore, the high-frequency sound cannot be accurately computed by using LES alone. However, the contribution from the small scales may be modeled separately and this is explored in the next section.

D. SGS Sound Radiation Model

One possible way to model the small-scale contribution to the Lighthill tensor is to assume that the small-scale motion can be modeled as homogeneous isotropic turbulence within each computational control volume of an LES, as suggested by Piomelli et al.[5] Turbulence theory can then be applied to estimate the far-field sound radiated by the removed small scales.[15] In this study, scale-similarity ideas were used to predict the contribution of the small scales to the sound source tensor. Among the scales removed by the filtering

operation, the largest scales play a relatively more important role for sound radiation than the smallest scales. The behavior of the largest of the unresolved scales could be modeled based on the smallest of the resolved scales. This is the idea behind scale-similarity SGS models and is depicted graphically in Fig. 10. Introducing a test filter whose width $\hat{\Delta}$ is larger than $\bar{\Delta}$, the model takes the form

$$T'_{ij} = T_{ij} - \bar{T}_{ij} = C(\bar{T}_{ij} - \hat{\bar{T}}_{ij}) \tag{22}$$

where C is a constant related to ratio of $\hat{\Delta}$ and $\bar{\Delta}$. The unfiltered Lighthill's stress tensor can then be approximated by

$$T_{ij} = \bar{T}_{ij} + C(\bar{T}_{ij} - \hat{\bar{T}}_{ij}) \tag{23}$$

The idea behind this model is depicted graphically in Fig. 10. The three curves in Fig. 10 are conceptual representations of the instantaneous energy spectrum functions for the Lighthill tensor from the DNS (solid line), $\bar{\Delta}$-filtered DNS (dashed line), and $\hat{\Delta}$-filtered DNS (dotted line). The vertical dashed and dotted lines represent the cut-off wave numbers for the $\bar{\Delta}$-filtered DNS and $\hat{\Delta}$-filtered DNS data, respectively. (Note that the axisymmetric flow in this study may not have similar spectra as shown in Fig. 10. The basic idea of the model, however, is still applicable to this flow.) The SGS sound model assumes that the energy level difference between the DNS and the $\bar{\Delta}$-filtered DNS is proportional to the energy level difference between the $\bar{\Delta}$-filtered DNS and $\hat{\Delta}$-filtered DNS. The T_{ij} components modeled with Eq. (23) are compared with the DNS results at two different frequencies in Fig. 11. In this comparison, $\bar{\Delta}$ and $\hat{\Delta}$ are selected as three and five times the grid spacing Δ_x, respectively, and the constant $C = 0.4$. In a more general formulation, the constant C could be evaluated by applying a dynamic modeling procedure.[16] The model predictions are in excellent agreement with the DNS results for both frequencies. Further tests of the model in the context of three-dimensional, high-Reynolds-number simulations with significant small-scale turbulence are needed, in conjunction with comparisons to laboratory measurements.

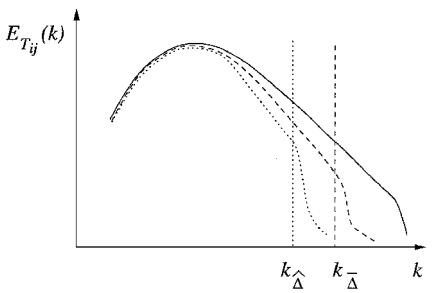

Fig. 10 Sketch depicting the idea behind the SGS sound radiation model showing a conceptual representation of the instantaneous energy spectrum functions for the Lighthill tensor from the ——, DNS; – – –, $\bar{\Delta}$-filtered DNS; and · · ·, $\hat{\Delta}$-filtered DNS.

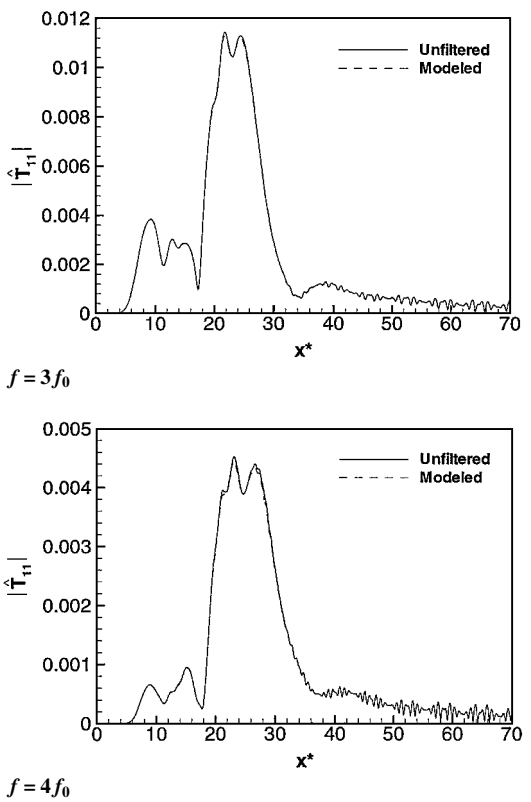

Fig. 11 Comparison of the magnitude of Lighthill's tensor component $\hat{\bar{T}}_{11}$ predicted by scale-similarity model and DNS results at two frequencies.

V. Conclusions

An a priori investigation of the effects of filtering on the sound generated by a subsonic axisymmetric jet was conducted. The direct numerical simulation results were in excellent agreement with previous numerical results in terms of the instantaneous and mean near-field jet flow structure and statistics and the far-field sound. The results were used to compute the Lighthill's tensor T_{ij} and its filtered counterpart $\bar{T}_{ij}$. Lighthill's acoustic analogy was implemented to predict the far-field sound. A novel approach based on spatial windowing was developed to minimize domain truncation errors and the Lighthill source term. For frequencies lower than twice the fundamental forcing frequency, the acoustic analogy predictions using both T_{ij} and $\bar{T}_{ij}$ were in good agreement with the directly computed sound, even at relatively shallow angles. For higher frequencies, the solution to Lighthill's equation was found to be inaccurate because refraction and dissipation effects on the sound inside the shear layer are not negligible. However, the magnitudes of the high-frequency components of $\bar{T}_{ij}$ were reduced by the filtering operation. This effect was satisfactorily addressed by modeling the SGS contribution to $\bar{T}_{ij}$ using scale-similarity ideas.

Acknowledgments

Funding for this research was provided by National Institutes of Health Grant DCO 3577-02 through an RO1 Grant from the National Institute on Deafness and Other Communication Disorders. Computational resources were provided by the National Center for Supercomputer Applications at the University of Illinois.

References

[1]Colonius, T., "Aeroacoustics and Active Noise Control: Lectures on Computational Aeroacoustics," von Kármán Inst. for Fluid Dynamics 1997-07, California Inst. of Technology, Pasadena, CA, 1997.

[2]Bastin, F., Lafon, P., and Candel, S., "Computation of Jet Mixing Noise due to Coherent Structures: The Plane Jet Case," *Journal of Fluid Mechanics*, Vol. 335, 1997, pp. 261–304.

[3]Gamet, L., and Estivalezes, J. L., "Application of Large-Eddy Simulation and Kirchoff Method to Jet Noise Prediction," *AIAA Journal*, Vol. 36, No. 12, 1998, pp. 2170–2178.

[4]Mitchell, B. E., Lele, S. K., and Moin, P., "Direct Computation of the Sound Generated by Vortex Pairing in an Axisymmetric Jet," *Journal of Fluid Mechanics*, Vol. 383, 1999, pp. 113–142.

[5]Piomelli, U., Street, C. L., and Sarkar, S., "On the Computation of Sound by Large-Eddy Simulations," *Journal of Engineering Mathematics*, Vol. 32, 1997, pp. 217–236.

[6]Seror, C., Sagaut, P., Bailly, C., and Juve, D., "Subgrid Scale Contribution to Noise Production in Decaying Isotropic Turbulence," AIAA Paper 99-1979, 1999.

[7]Lighthill, M. J., "On Sound Generated Aerodynamically; I. General Theory," *Proceedings of the Royal Society of London*, Vol. A211, 1952, pp. 564–587.

[8]Boersma, B. J., and Lele, S. K., "Large-Eddy Simulation of a Mach 0.9 Turbulent Jet," AIAA Paper 99-1874, 1999.

[9]Lele, S. K., "Compact Finite-Difference Schemes with Spectral-Like Resolution," *Journal of Computational Physics*, Vol. 103, No. 1, 1992, pp. 16–42.

[10]Thompson, K. W., "Time-Dependent Boundary Conditions for Hyperbolic Systems," *Journal of Computational Physics*, Vol. 68, No. 1, 1987, pp. 1–24.

[11]Colonius, T., Lele, S. K., and Moin, P., "Boundary Conditions for Direct Computation of Aerodynamic Sound Generation," *AIAA Journal*, Vol. 31, No. 9, 1993, pp. 1574–1582.

[12]Michalke, A., and Hermann, G., "On the Inviscid Instability of a Circular Jet with External Flow," *Journal of Fluid Mechanics*, Vol. 114, 1982, pp. 343–544.

[13]Colonius, T., Lele, S. K., and Moin, P., "Sound Generation in a Mixing Layer," *Journal of Fluid Mechanics*, Vol. 330, 1997, pp. 375–409.

[14]Lilley, G. M., "Jet Noise Classical Theory and Experiments," *Aeroacoustics of Flight Vehicles: Theory and Practice*, edited by H. H. Hubbard, Acoustical Society of America, Woodbury, NY, 1995, pp. 211–285.

[15]Proudman, I., "The Generation of Sound by Isotropic Turbulence," *Proceedings of the Royal Society of London*, Vol. A214, 1952, pp. 119–132.

[16]Germano, M., Piomelli, U., Moin, P., and Cabot, W. H., "A Dynamic Subgrid-Scale Eddy Viscosity Model," *Physics of Fluids A*, Vol. 3, No. 7, 1991, pp. 1760–1765.

P. J. Morris
Associate Editor